

Electrochemical Study of Hydrogen Peroxide Detection on MnO₂ Micromaterials

Lili Feng*, Rui Wang, Yulu Shi, Hongbin Wang, Jianhua Yang, Jiang Zhu, Yan Chen, Na Yuan

Key Laboratory of Resource Clean Conversion in Ethnic Regions, Education Department of Yunnan, Yunnan Minzu University, Kunming 650500, China

*E-mail: lilylian2003@163.com

Received: 25 March 2016 / Accepted: 11 May 2016 / Published: 4 June 2016

Herein we report that urchin-like MnO₂ micromaterials, caddice-clew like MnO₂ micromaterials and MnO₂ nanoflowers were prepared by hydrothermal method. All the crystalline phases were α -MnO₂, which was essential to evaluate the relationship between electrochemical performances and morphologies of MnO₂ crystals for H₂O₂ detection. The value of H₂O₂ oxidation peak current on all the MnO₂ crystals modified electrode were all much higher than glassy carbon electrode. The performances of H₂O₂ detection were in the following order: urchin-like MnO₂ micromaterials > MnO₂ nanoflowers > caddice-clew like MnO₂ micromaterials. Here more electro-activity sites might be the most important factor of the increased oxidation peak current. The redox processes of H₂O₂ on all the three MnO₂ sample modified electrodes were controlled by diffusion. The results presented in this study that the as prepared MnO₂ materials have good application prospect in detecting H₂O₂.

Keywords: Electro-analysis, Manganese dioxide, Hydrothermal method, Hydrogen peroxide

1. INTRODUCTION

Hydrogen peroxide is a very important intermediate in environmental and biological reactions and is widely applied in industrial processes as a universal oxidant. The monitoring of H₂O₂ with a reliable, rapid, and economic method is of great significance in many different fields, such as food, clinical, pharmaceutical, industrial and environmental analysis. Electroanalytical method has many advantages in detecting H₂O₂, such as low-cost, high sensitivity, reliability, operational simplicity and rapid response time. Therefore, a number of studies have been carried out to find out good catalytic substance to promote the decomposition of H₂O₂ using in electroanalytical method.

Nowadays, with the development of nanoscience and nanotechnology, nanomaterials usually play an important role in improving electroanalytical performance due to their large specific surface

areas and biocompatibilities. Up to now, various MnO_2 crystals with different morphologies such as nanosphere[1, 2], nanorod[3, 4], nanoflower[4, 5], nanotube[6], urchin-like morphology and caddice-clew-like morphology[7], hollow structure[8, 9] had been synthesized. Manganese dioxides nanomaterials with diverse crystal morphologies are widely used in catalysis, biosensors, water treatment, electrochemical supercapacitors. Because of the good catalytic properties, manganese dioxide is one of the most promising candidates to detect H_2O_2 [10-15]. For examples, Wei-De Zhang et al. fabricated a highly sensitive amperometric sensor based on MnO_2 modified vertically aligned multiwalled carbon nanotubes ($\text{MnO}_2/\text{VACNTs}$) for determination of hydrogen peroxide. The sensor was applied for the determination of trace of H_2O_2 in milk with high accuracy[11]. Jilie Kong et al. fabricated a nonenzymatic hydrogen-peroxide sensor using the graphene, carbon nanotube and MnO_2 hybrid as the sensing material[10]. The sensor exhibited extremely high electrocatalytic activity toward the oxidation of H_2O_2 with a low detection limit of $0.1\mu\text{M}$.

The research on MnO_2 detection was relatively complex because MnO_2 exist several crystallographic forms such as α -, β -, γ -, and δ -type. For examples, K. Justice Babu et al. had prepared rod, belt, and flower shape MnO_2 nanomaterials with different phases[16]. The prepared MnO_2 nanostructures exhibited good electrocatalytic activities in detecting the hydrogen peroxide. Among the studied nanostructures, γ - MnO_2 exhibited an excellent sensing behavior toward hydrogen peroxide. But here the crystallographic forms and the different morphologies had a comprehensive influence. R.B. Valim et al. studied the oxygen reduction reaction on carbon supported epsilon manganese dioxide (ϵ - MnO_2/C)[17]. The higher amount of hydrogen peroxide detected on the ORR catalyzed by ϵ - MnO_2/C than α - MnO_2 . So, from the above two examples we could summarize that the electrochemical performance of MnO_2 crystals had relationship both with the crystallographic forms and with the morphologies. Therefore, the researches on the relationship of electrochemical performance with the morphologies and the relationship of electrochemical performance with the crystallographic forms were very essential.

The aims of the present work are to synthesize α - MnO_2 with three different morphologies such as urchin-like MnO_2 micromaterials, caddice-clew like MnO_2 micromaterials and MnO_2 nanoflowers by hydrothermal method, and to fabricate a modified electrodes to detect H_2O_2 by simple cast method, and then to investigate the relationship between electrochemical performances and morphologies.

2. EXPERIMENTAL SECTION

2.1 Synthesis and Characterization of MnO_2 Micromaterials Prepared by Hydrothermal Method

All reagents purchased from the Shanghai Chemical Company were of analytical grade, and used without further purification. The preparation of caddice-clew-like MnO_2 micromaterial was as follows: 1.70 g $\text{MnSO}_4 \cdot \text{H}_2\text{O}$ was dissolved in 15 mL distilled water with vigorous stirring. When the solution was clear, 20 mL aqueous solution containing 2.72g $\text{K}_2\text{S}_2\text{O}_8$ were added to the above solution under continuous stirring. Then the resulting transparent solution was transferred into a Teflon-lined stainless steel autoclave (50 mL) of 80% capacity of the total volume. The autoclave was sealed and

maintained at 110 °C for 6 h. After the reaction was completed, the autoclave was allowed to cool to room temperature naturally. The solid black precipitate was filtered, washed several times with distilled water to remove impurities, and then dried at 80 °C in air for 3 hours. The obtained caddice-clew-like MnO₂ micromaterial was collected for the following characterization.

In this study, other MnO₂ micromaterials were prepared by the similar method, while the concentration of the reagents was adjusted. The detailed data were shown in table 1.

The morphological investigations of SEM images were taken on a field emission scanning electron microscope (FESEM, Zeiss Ultra). The crystallographic structures of the products were determined with XRD which were recorded on a Rigaku D/max-2200/PC with Cu target at a scanning rate of 7°/min with 2θ ranging from 10 to 70°.

Table 1. Experimental condition for MnO₂ samples in this work

Expt.	MnSO ₄ (g)	K ₂ S ₂ O ₈ (g)	H ₂ SO ₄ (mL)	Temperature °C	Time h
a	0.3415	0.5434	2	110	6
b	0.3415	0.5434	0	110	6
Expt.	MnSO ₄ (g)	KMnO ₄ (g)		Temperature °C	Time h
c	0.2	0.5		110	6

2.2 Electrochemical Studies of MnO₂ Micromaterials

Electrochemical measurements were all operated on a CHI 604E electrochemical workstation (Chenhua Co., Shanghai, China) in a conventional three-electrode cell, which includes a saturated calomel electrode (SCE) as reference electrode, a platinum electrode (1cm x 1cm) as counter electrode, and a bare or modified glassy carbon electrode (GCE, 3 mm in diameter) as working electrode. Before testing, the glassy carbon electrode was rejuvenated by polishing with 0.3 μm and 0.05 μm alumina powder respectively and sonicating sequentially in alcohol, deionized water in each for about 20 min. Then, The modified GCE was fabricated by casting 5 μL of the desired solution containing MnO₂ micromaterials, after drying, 5 μL of 0.5 wt.% Nafion solution was casted on the surface. Phosphate buffer solution (PBS, 0.2 M, pH 7.0) is used as supporting electrolyte, and high-purity nitrogen was bubbled for 20 min prior to starting the experiments. In this study, the concentration of hydrogen peroxide solution was calibrated with potassium permanganate solution (0.02 mol L⁻¹). Cyclic voltammogram (CV) tests were carried out from 0 to 1.00 V. Amperometric i-t curve tests were carried out at 0.8V.

3. RESULTS AND DISCUSSION

3.1 Structure and Morphology

Fig. 1 displayed the SEM images of the MnO₂ micro-nano materials. As shown in Fig. 1a, the MnO₂ material was sea-urchin like morphology with uniform diameter. The urchin-like MnO₂ were

assembled from needle-like nanorods that were about 1 μm in length. As can be seen, the urchin-like MnO_2 microsphere had hollow interior. The whole diameter of the urchin-like MnO_2 micro-nano materials was about 3 μm for average. In Fig. 1b MnO_2 micro-nano wires were formed. These nanowires aggregated into spherical shape, and looked like a caddice-clew. The nanowires were about 55-83 nm in width and were several micrometers in length for average. Fig. 1c showed the samples exhibit flower shape structures with diameters of about 800-1200 nm. The individual MnO_2 nanoflower was composed by a large number of thin nanosheets with about 10-20 nm thickness.

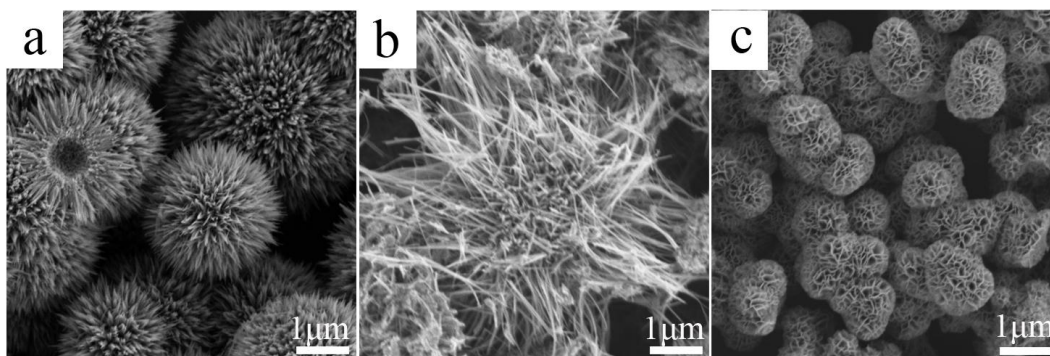


Figure 1. SEM images of MnO_2 samples. (a) (b) (c) are consistent with that listed in Table 1.

The XRD patterns of the MnO_2 micro-nano materials were shown in Fig. 2. As shown, the three samples had similar crystallographic structure. The diffraction peaks appeared at $2\theta=12.7^\circ$, 18.1° , 28.8° , 37.5° , 42.1° , 49.9° , 56.2° , 60.3° matched well with the diffraction peaks of (110), (200), (310), (211), (301), (411), (600) and (521) crystal planes of $\alpha\text{-MnO}_2$ standard data (JCPDS card PDF file No. 44-0141). According to the literature, when MnO_2 nanoflowers prepared at 180°C for 24 h, the MnO_2 sample was birnessite-type, and denoted as $\delta\text{-MnO}_2$. Here when we prepared MnO_2 sample at 110°C for 6 h, the MnO_2 nanoflowers were $\alpha\text{-MnO}_2$. So we think the synthetic temperature and time were very important to the crystallographic structure of MnO_2 .

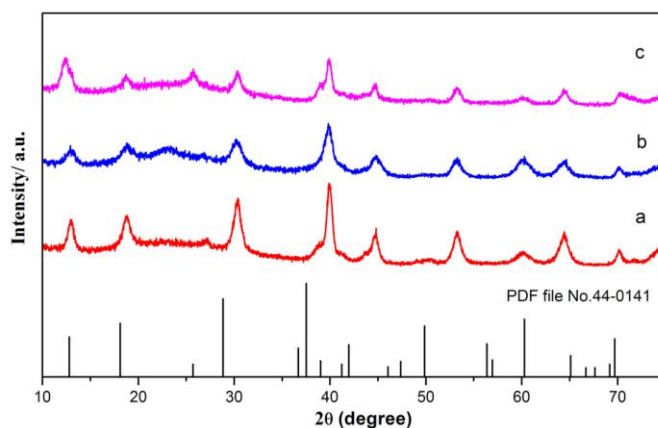


Figure 2. The XRD patterns of MnO_2 materials. (a) (b) (c) are consistent with that listed in Table 1.

3.2 Electrochemical Performance

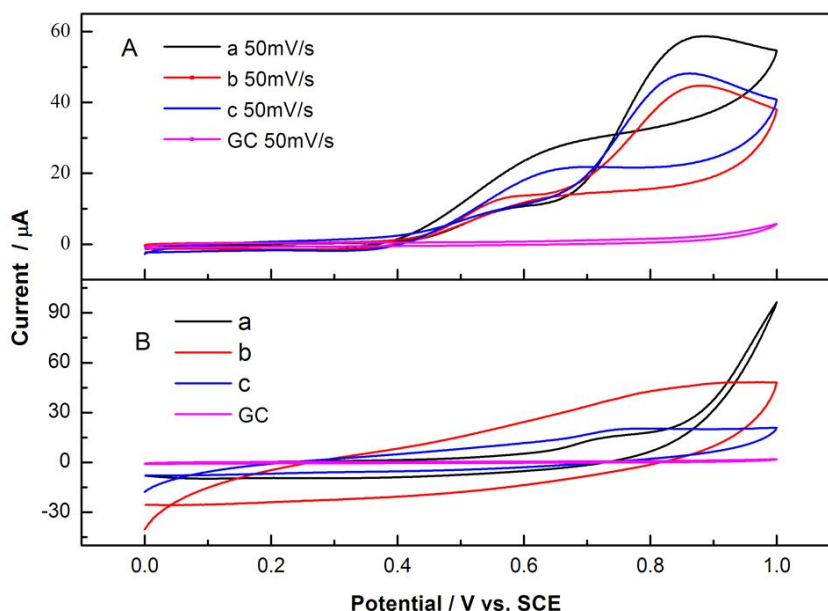
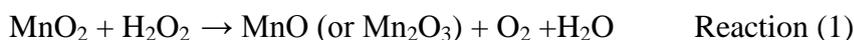


Figure 3. (A) Cyclic voltammetric curves of 5mmol L⁻¹ H₂O₂ in 0.2 mol L⁻¹ PBS (pH=7.0) on a) sample a modified electrode, b) sample b modified electrode, c) sample c modified electrode, d) glassy carbon(GC) electrode. Scan rate: 50 mV s⁻¹. (B) Cyclic voltammetric curves in 0.2 mol L⁻¹ PBS on a) sample a modified electrode, b) sample b modified electrode, c) sample c modified electrode, d) glassy carbon(GC) electrode. Scan rate: 50 mV s⁻¹.

Cyclic voltammetry (CV) was used to study the electrocatalytic activity of various MnO₂ materials for the detection of H₂O₂. Fig. 3A showed the cyclic voltammetric curves of 5 mmol L⁻¹ H₂O₂ in 0.2 mol L⁻¹ PBS on glass carbon (GC) electrode and the samples modified electrodes at 50 mV s⁻¹. Fig. 3B was the blank cyclic voltammetric curves of the glass carbon (GC) electrode and the samples modified electrodes. As shown in Fig. 3A, H₂O₂ oxidation peaks were clearly observed at 0.86 V in the forward sweep and at 0.64 V in the backward sweep of the three MnO₂ materials modified electrode. In contrast, the H₂O₂ oxidation peaks were not obvious on the bare glassy carbon (GC) electrode. According to the Ref.[10-12], it was assigned to the reduction of MnO₂ to Mn²⁺ or Mn³⁺ and the reoxidation of Mn²⁺ or Mn³⁺ back to MnO₂. In the presence of H₂O₂, the CV displayed a very significant oxidative current at potentials between 0.5V and 1.0V. The possible electrocatalytic mechanism may undergo the following steps. Firstly, H₂O₂ was adsorbed on the surface of MnO₂/GCE; secondly, MnO₂ was reduced to lower states by the absorbed H₂O₂; thirdly, lower states of Mn were electro-oxidized back to MnO₂ on the electrode surface.



As shown in Fig. 3A, Sample a (urchin-like MnO₂) modified electrode has the biggest value of H₂O₂ oxidation peak current. The value of H₂O₂ oxidation peak current of sample c (MnO₂ nanoflowers) modified electrode was a little lower than sample a modified electrode. Sample b (caddice-clew like MnO₂) modified electrode has the lowest value of H₂O₂ oxidation peak current

among the three MnO₂ materials modified electrode. In general, the increased oxidation peak current was usually resulted from the better conductivity, the higher specific area or more active catalytic sites of the modified material. Firstly, As for MnO₂ material belongs to semiconductor, the conductivity of the MnO₂ materials modified electrode should be poorer than the bare glassy carbon (GC) electrode. So the increased oxidation peak current of the MnO₂ material modified electrode should not due to the conductivity of the sample. Secondly, in Fig. 3B, sample *b* modified electrode had the highest blank current, as a result, sample *b* modified electrode should have the biggest specific area. However sample *b* modified electrode had the lowest value of H₂O₂ oxidation peak current among the three MnO₂ materials modified electrode. So in this study, the enhanced performance of the MnO₂ materials modified electrode was not due to good conductivity and higher specific area of the MnO₂ materials. Finally the performance of the MnO₂ materials modified electrode may attribute to more electro-activity sites. According to the high oxidation peak current in Fig. 3A, sample *a* (urchin-like MnO₂) maybe have more electro-activity sites among the three samples.

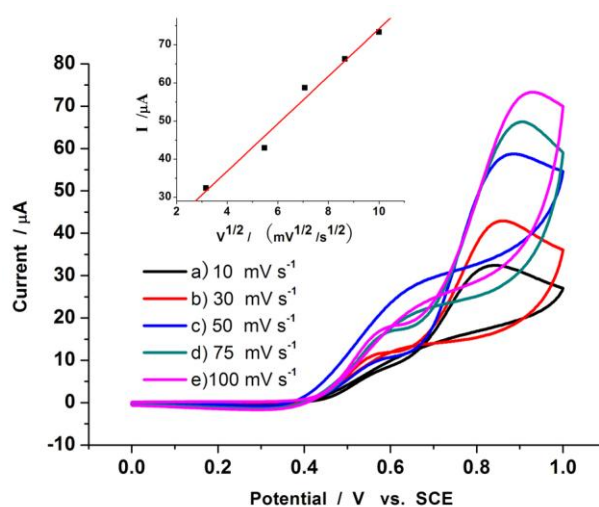


Figure 4. Cyclic voltammetric curves for sample a (urchin-like MnO₂ microsphere modified electrode) of 5 mmol L⁻¹ H₂O₂ in 0.2 mol L⁻¹ PBS (pH=7.0) at different scan rates: (a) 10, (b) 30, (d) 50, (e) 75, (f) 100 (mV s⁻¹). Inset: The relation between anodic peak currents of H₂O₂ versus the square root of scan rate.

We explored the relationship between oxidation peak current in the forward sweep with scan rate for urchin-like MnO₂ microsphere modified electrode (sample a). The results were in Fig. 4. As shown, the oxidation peak currents were proportional to the square root of scan rate in the range 10-100 mV s⁻¹. The correlation coefficient for sample *a* was 0.992.

The relationship between oxidation peak current in the forward sweep with scan rate for caddice-clew like MnO₂ micromaterials modified electrode (sample b) were shown in Fig. 5. The oxidation peak currents were proportional to the square root of scan rate in the range 10-100 mV s⁻¹. The correlation coefficient for sample *b* was 0.996.

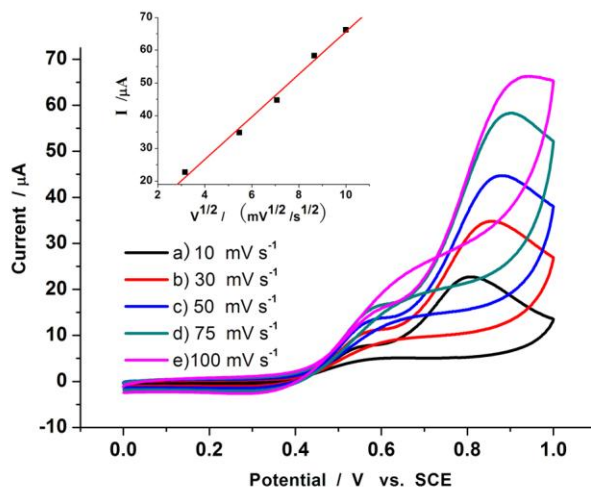


Figure 5. Cyclic voltammetric curves for sample b (caddice-clew like MnO_2 micromaterials modified electrode) of 5mmol L^{-1} H_2O_2 in 0.2 mol L^{-1} PBS (pH=7.0) at different scan rates: (a) 10, (b) 30, (d) 50, (e) 75, (f) 100 (mV s^{-1}). Inset: The relation between anodic peak currents of H_2O_2 versus the square root of scan rate.

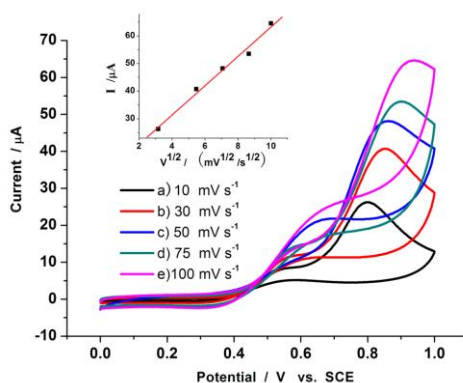


Figure 6. Cyclic voltammetric curves for sample c (MnO_2 nanoflowers modified electrode) of 5mmol L^{-1} H_2O_2 in 0.2 mol L^{-1} PBS (pH=7.0) at different scan rates: (a) 10, (b) 30, (d) 50, (e) 75, (f) 100 (mV s^{-1}). Inset: The relation between anodic peak currents of H_2O_2 versus the square root of scan rate.

The relationship between oxidation peak current in the forward sweep with scan rate for MnO_2 nanoflowers modified electrode (sample c) were shown in Fig. 6. The oxidation peak currents were proportional to the square root of scan rate in the range $10\text{--}100\text{ mV s}^{-1}$. The correlation coefficient for sample c was 0.993.

For all the three samples, the oxidation peak currents were proportional to the square root of scan rate. These indicated that the redox processes of H_2O_2 on all the three MnO_2 sample modified electrodes were controlled by diffusion. So the performances of H_2O_2 detection were not decided by the electrochemical process. As mentioned above, the conductivity and specific area of the sample and the electrochemical process did not have a decisive effect on the enhanced performance of the MnO_2

materials modified electrode, so the performance of the MnO₂ materials modified electrode may attribute to more electro-activity sites of the MnO₂ materials.

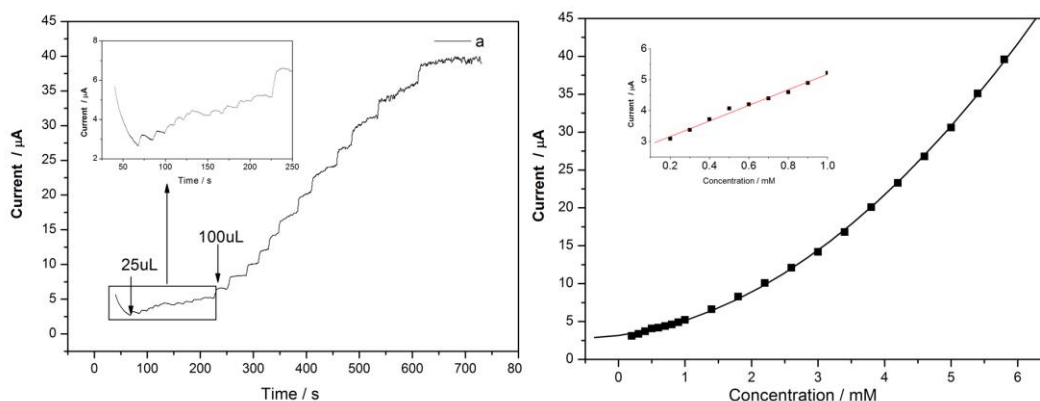


Figure 7. Current-time response of sample *a* modified electrode upon addition of H₂O₂ at 0.8 V. Cell volume: 20 mL; firstly added H₂O₂ solution 25µL(10th) (0.08mol L⁻¹); then added H₂O₂ solution 100µL(10th) (0.08mol L⁻¹).

The relationship between the oxidation current and the concentration of H₂O₂ was examined. **Figure 7** shows typical current-time response of sample *a* modified electrode to the continuous addition of H₂O₂ in PBS solution (pH=7.0) at 0.8 V. It is observed that sample *a* modified electrode has a relatively quick response to the change of H₂O₂ concentration. But it needs some time to reach a steady-state signal. The current signal is linear with the concentration in the range from 0.1mmol L⁻¹ to 1.0 mmol L⁻¹, and the correlation factor of the straight line was 0.995. After added H₂O₂ solution to 1.0m mol L⁻¹, the current signal increase rapidly. The detection limit of sample *a* modified electrode here was 1.13x10⁻⁶ mol L⁻¹ (S/N=3).

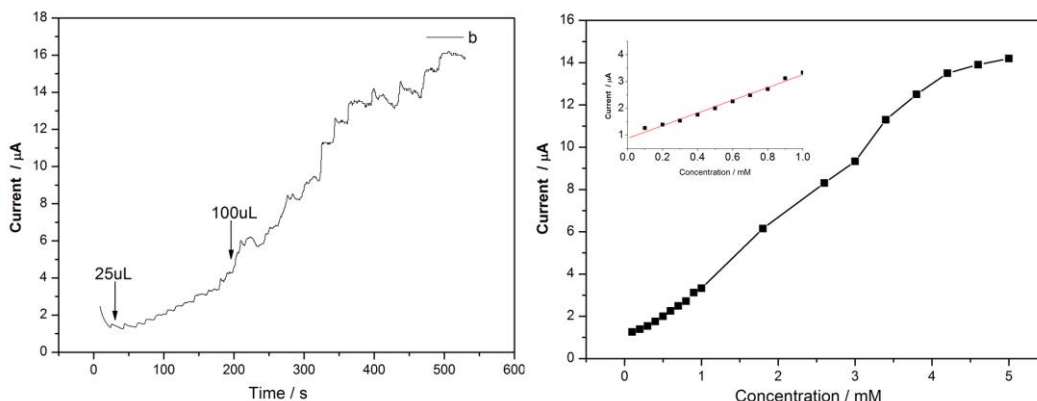


Figure 8. Current-time response of sample *b* modified electrode upon addition of H₂O₂ at 0.8 V. Cell volume: 20 mL; firstly added H₂O₂ solution 25µL(10th) (0.08mol L⁻¹); then added H₂O₂ solution 100µL(10th) (0.08mol L⁻¹).

Figure 8 shows the current-time response of sample *b* modified electrode to the continuous addition of H₂O₂ in PBS solution (pH=7.0) at 0.8 V. The current-time response is similar to sample *a*

modified electrode. The current signal is linear with the concentration in the range from 0.1 mmol L^{-1} to 1.0 mmol L^{-1} , and the correlation factor of the straight line was 0.994. Here the current intensity is much lower than sample *a* modified electrode. The detection limit of sample *b* modified electrode here was $1.29 \times 10^{-6} \text{ mol L}^{-1}$ (S/N=3).

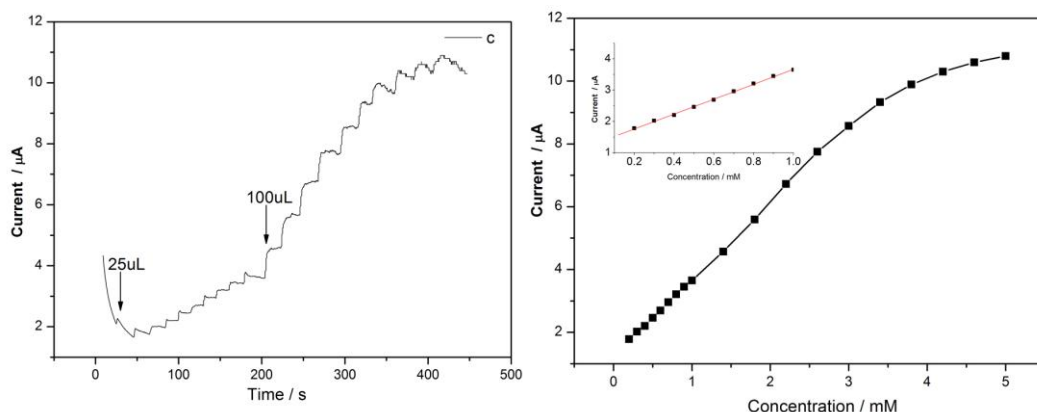


Figure 9. Current-time response of sample *c* modified electrode upon addition of H_2O_2 at 0.8 V. Cell volume: 20 mL; firstly added H_2O_2 solution 25 μL (10^{th}) (0.08 mol L^{-1}); then added H_2O_2 solution 100 μL (10^{th}) (0.08 mol L^{-1}).

Figure 9 is the current-time response of sample *c* modified electrode to the continuous addition of H_2O_2 in PBS solution (pH=7.0) at 0.8 V. The current-time response is similar to sample *a* modified electrode too. The current signal is linear with the concentration in the range from 0.1 mmol L^{-1} to 1.0 mmol L^{-1} , and the correlation factor of the straight line was 0.999. Here the current intensity is much lower than sample *a* modified electrode. The detection limit of sample *a* modified electrode here was $1.84 \times 10^{-6} \text{ mol L}^{-1}$ (S/N=3).

From all the electrochemical data above, the electrochemical performances of the MnO_2 micromaterials exactly had relationship on their morphologies. Among the three MnO_2 samples, urchin-like MnO_2 micromaterials modified electrode had the best performance of H_2O_2 detection such as the biggest H_2O_2 oxidation peak current, the lowest detection limit ($1.13 \times 10^{-6} \text{ mol L}^{-1}$). In literature [12], the MnO_2/Au composite film had an improved electrocatalytic activity for oxidation of H_2O_2 and the detection limit was estimated to be $1 \times 10^{-6} \text{ mol L}^{-1}$ (S/N=3). Compared to our results, the detection limit was almost similar. In general, Au shell coating could enhance the conductivity, so it is a strategy to improve the H_2O_2 oxidation peak current of our MnO_2 samples. In literature [10], the hybrid of $\text{MnO}_2/\text{graphene}/\text{carbon nanotubes}$ had a low detection limit of $0.1 \times 10^{-6} \text{ mol L}^{-1}$. This report is slightly better than our results. Here the doped graphene could enhance the conductivity, so the performance of H_2O_2 detection was better. In addition, the detection limit in literature [14] was $1.12 \times 10^{-6} \text{ mol L}^{-1}$, in literature [18] was $2.45 \times 10^{-6} \text{ mol L}^{-1}$, the results were almost similar to ours. On the base of several literature, especially literature [16] ($\gamma\text{-MnO}_2$ exhibited an excellent sensing behaviour and the detection limit was $0.1 \times 10^{-6} \text{ mol L}^{-1}$), our results enriched the relationship between electrochemical performances of the MnO_2 micromaterials and their morphologies.

4. CONCLUSION

In conclusion, urchin-like MnO₂ micromaterials, caddice-clew like MnO₂ micromaterials and MnO₂ nanoflowers were prepared by hydrothermal method. All the crystalline phases were α -MnO₂, which was essential to evaluate the relationship between electrochemical performances and morphologies of MnO₂ crystals for H₂O₂ detection. The value of H₂O₂ oxidation peak current on all the MnO₂ crystals modified electrode were all much higher than glassy carbon electrode. The performances of H₂O₂ detection were in the following order: urchin-like MnO₂ micromaterials > MnO₂ nanoflowers > caddice-clew like MnO₂ micromaterials. Among the MnO₂ materials modified electrode, more electro-activity sites might be the most important factor of the increased oxidation peak current. The results presented in this research that the as prepared MnO₂ materials have good application prospect in detecting H₂O₂.

ACKNOWLEDGEMENTS

This work was financially supported by Program for National Natural Scientific Fund (No.21463028, No.215650312), YMU-DEAKIN International Associated Laboratory on Functional Materials, Key Laboratory of Resource Clean Conversion in Ethnic Region, Education Department of Yunnan Province (117-02001001002107), the general program of the application and basic research foundation of Yunnan province (2013FZ080), and Innovative Training Program of Yunnan Minzu University for Undergraduates.

References

1. M. Xu, L. Kong, W. Zhou, H. Li, *J. Phys. Chem. C*, 111 (2007) 19141-19147.
2. Z. Li, Y. Ding, Y. Xiong, Y. Xie, *Crystal Growth & Design*, 5 (2005) 1953-1958.
3. X. Wang, Y. Li, *Chem. Commun.*, (2002) 764-765.
4. X. Duan, J. Yang, H. Gao, J. Ma, L. Jiao, W. Zheng, *Cryst. Eng. Comm.*, 14 (2012) 4196-4204.
5. W.N. Li, J. Yuan, X.F. Shen, S. Gomez-Mower, L.P. Xu, S. Sithambaram, M. Aindow, S.L. Suib, *Adv. Funct. Mater.*, 16 (2006) 1247-1253.
6. L. Li, C. Nan, J. Lu, Q. Peng, Y. Li, *Chem. Commun.*, 48 (2012) 6945-6947.
7. L. Feng, Z. Xuan, H. Zhao, Y. Bai, J. Guo, C. Su, *Nanoscale Res. Lett.*, 9 (2014) 290.
8. J. Fei, Y. Cu, X. Yan, W. Qi, Y. Yang, K. Wang, Q. He, J. Li, *Adv. Mater.*, 20 (2008) 452-456.
9. D. Portehault, S. Cassaignon, E. Baudrin, J.P. Jolivet, *Crystal Growth & Design*, 9 (2009) 2562-2565.
10. D. Ye, H. Li, G. Liang, J. Luo, X. Zhang, S. Zhang, H. Chen, J. Kong, *Electrochimica Acta*, 109 (2013) 195-200.
11. B. Xu, M.L. Ye, Y.X. Yu, W.D. Zhang, *Analytica Chimica Acta*, 674 (2010) 20-26.
12. Y.J. Yang, S. Hu, *Electrochimica Acta*, 55 (2010) 3471-3476.
13. Y. Li, J. Zhang, H. Zhu, F. Yang, X. Yang, *Electrochimica Acta*, 55 (2010) 5123-5128.
14. X. Xiao, Y. Song, H. Liu, M. Xie, H. Hou, L. Wang, Z. Li, *J. Mater. Sci.*, 48 (2013) 4843-4850.
15. S. Yao, J. Xu, Y. Wang, X. Chen, Y. Xu, S. Hu, *Analytica Chimica Acta*, 557 (2006) 78-84.
16. K.J. Babu, A. Zahoor, K.S. Nahm, R. Ramachandran, M.A.J. Rajan, G.G. kumar, *J. Nanopart. Res.*, 16 (2014) 2250.
17. R.B. Valim, M.C. Santos, M.R.V. Lanza, S.A.S. Machado, F.H.B. Lima, M.L. Calegari, *Electrochimica Acta*, 85 (2012) 423-431.

18. A.J. Wang, P.P. Zhang, Y.F. Li, J.J. Feng, W.J. Dong, and X.Y. Liu, *Microchim Acta*, 175 (2011) 31-37.

© 2016 The Authors. Published by ESG (www.electrochemsci.org). This article is an open access article distributed under the terms and conditions of the Creative Commons Attribution license (<http://creativecommons.org/licenses/by/4.0/>).